Ocean Engineering 338 (2025) 121952

Contents lists available at ScienceDirect

Ocean Engineering

journal homepage: www.elsevier.com/locate/oceaneng

Research paper

Impact of leeway and rudder angles on ship resistance: A numerical planar motion mechanism approach

Burak Göksu [a,b,*], Suraj Garad [b,c], Stefano Pandini [d], Edoardo Sirolla [d], Robert Palin [d], Nicholas Townsend [b], Tahsin Tezdogan [b]

[a] Department of Marine Engineering, Maritime Faculty, Zonguldak Bulent Ecevit University, Zonguldak, Turkey
[b] Department of Civil, Maritime and Environmental Engineering, Faculty of Engineering and Physical Science, School of Engineering, University of Southampton, Southampton, UK
[c] Department of Ocean Engineering and Naval Architecture, Indian Institute of Technology, Kharagpur, India
[d] Spaera Ltd, London, UK

ARTICLE INFO

Keywords:
Computational fluid dynamics (CFD)
Leeway angle
Ship resistance
Wind-assisted propulsion
Wave resistance

ABSTRACT

Driven by environmental policies, the maritime sector is increasingly utilising sustainable energy sources, with wind energy emerging as a primary strategy for achieving zero-carbon emissions. These wind-propulsion devices augment the ship's propulsion, while the lateral force they generate causes a yawing moment that induces a leeway angle and added resistance. This study uses computational fluid dynamics (CFD) simulations to investigate the hydrodynamic behaviour of a ship at various leeway and rudder angles. It also examines how the leeway angle affects the wave-making resistance coefficient at different speeds. Model-scale evaluations were first performed with 0° rudder and 0° leeway (straight-ahead) at ship speeds from 8 to 14 knots. Then, the effects of various leeway and rudder angles were investigated at 11 and 14 knots. The combination of a 10° leeway angle with a 20° rudder angle was identified as the worst-case scenario, causing approximately a 100 % increase in total resistance at 11 knots and a 40 % increase at 14 knots in calm water. Understanding the hydrodynamic behaviour under these conditions is crucial for improving ship design and operational strategies, ultimately contributing to zero-carbon maritime transportation goals.

1. Introduction

1.1. Context

In the field of maritime transportation, striving for efficiency and optimal vessel performance remains an ongoing effort. The resistance encountered by a ship as it moves through water is a significant factor that affects fuel efficiency, travel time, and operational expenses. Naval architects and marine engineers endeavour to reduce resistance by employing advanced hull designs, propulsion systems, and operational methodologies. However, providing accurate predictions and reducing resistance requires an in-depth understanding of the complex interactions between a vessel and its surrounding environment.

Simultaneously, environmental regulations are pushing the maritime industry to minimise its carbon footprint. The International Maritime Organization (IMO) regulatory framework plays a crucial role in encouraging the adoption of greener technologies and enhancing operational efficiency in practices. Shipowners must now adopt the Ship Energy Efficiency Management Plan (SEEMP), which details specific energy-saving measures and vessel adjustments to adhere to IMO regulations (Yalama et al., 2022). To achieve international sustainability targets, the integration of technological advancements with renewable energy solutions is essential. For example, wind-assisted propulsion systems (WAPS) may enable the maritime industry to meet these goals (Chou et al., 2021; Oduro et al., 2024).

1.2. Literature review and scientific challenges

Wind-assisted propulsion systems (WAPS), such as Flettner rotors, wing sails, and kites, are being incorporated into ships to decrease fuel consumption and emissions. WAPS technologies utilise wind energy to propel vessels, leading to significant fuel savings and reduced emissions.

* Corresponding author. Department of Marine Engineering, Maritime Faculty, Zonguldak Bulent Ecevit University, Zonguldak, Turkey.
E-mail addresses: burakgoksu@beun.edu.tr, b.goksu@soton.ac.uk (B. Göksu), s.garad@soton.ac.uk (S. Garad), stefano.pandini@spaera.eco (S. Pandini), edoardo.sirolla@spaera.eco (E. Sirolla), rob.palin@spaera.eco (R. Palin), n.c.townsend@soton.ac.uk (N. Townsend), t.tezdogan@soton.ac.uk (T. Tezdogan).

https://doi.org/10.1016/j.oceaneng.2025.121952
Received 14 March 2025; Received in revised form 1 June 2025; Accepted 17 June 2025
Available online 27 June 2025

For instance, Talluri et al. (2018) carried out a case study on a merchant vessel equipped with Flettner rotors, indicating that the implementation of these rotors could lead to a reduction of fuel costs by as much as 20 %, along with a notable decrease in CO_2 and NO_x emissions. Furthermore, Pradana et al. (2022) emphasised that the fuel savings achieved through Flettner rotors can vary from 0.4 % to as high as 50 %, influenced by different environmental factors including wind angle and velocity. Additionally, a study conducted by Seddiek and Ammar (2021) illustrated that Flettner rotors have the potential to achieve annual fuel savings of as much as 22.28 % for bulk carriers. This is consistent with the findings from the Enercon E-Ship 1, which realised fuel savings of around 22.9 %, following the installation of four Flettner rotors (Schmidt, 2013). In a case study by Issa et al. (2022), for a vessel routed across the Adriatic Sea, possible fuel savings were analysed using wind data from Copernicus Marine Services. From the wind data of the route, it was concluded that an average of 12.5 % in fuel reduction is possible if calculated using monthly mean wind values. Furthermore, it was found in another study that the aerodynamic efficiency of the wingsails is critical to gain a meaningful thrust contribution (Viola et al., 2015). Wang et al. (2022) presented that the propeller thrust decreased by about 10 % when sailing crosswind, and the maximum benefit was achieved by sailing at low speed in strong wind conditions.

Improvements in control systems and vessel design are enhancing these technologies for different wind conditions. To maximise the advantages of the aerodynamic forces generated by WAPSs, Dupuy et al. (2023) analysed both the forces affecting ship hydrodynamics and those contributing to propulsion benefits through route optimisation. Upon examining Flettner rotors, suction wings, and wing sails individually, they found that the Flettner rotor yielded the most favourable results in the optimisation process. Werner et al. (2023) emphasised that optimising the design of wind-assisted propulsion systems—aimed at enhancing energy efficiency and reducing carbon emissions on ships—requires a comprehensive evaluation of aerodynamic, hydrodynamic, control, routing, and logistical processes in an integrated manner. Accordingly, they argued that new designs necessitate more complex decision-making mechanisms compared to retrofit systems. Thies and Ringsberg (2023) highlighted the importance of WAPS device placement and the non-linear benefits of high lift-to-drag sails in larger systems. Key factors for accurate predictions include sail lift, hull drift drag, and wind angle. In conclusion, they emphasised that the impact of a large sail area on drift uncertainties represents a particularly complex aspect of WAPS design. However, a key disadvantage of wind-assisted propulsion systems is their tendency to generate a leeway angle during cruising due to the lateral forces (Charlou et al., 2023), which then necessitates rudder deflections to maintain course.

The leeway angle is a critical hydrodynamic parameter: it alters the hull's effective angle of attack, which in turn changes the pressure distribution on the hull surface and modifies flow patterns and drag (Elger et al., 2020; Galić et al., 2022; Sun et al., 2015). Experimental investigations also show that an increase in rudder angle results in an overall increase in ship resistance (Bi et al., 2024; Lu et al., 2023). However, in practice, the dynamics of this relationship are further complicated by the presence of the propeller, which significantly influences the flow conditions encountered by the rudder through its wake. The interaction may result in complex flow phenomena, including vortex shedding and cavitation, which can negatively impact the functionality of both the rudder and the propeller (Lu et al., 2023; Song et al., 2022), resulting in both increased resistance and suboptimal manoeuvring (Park et al., 2021; Sunarsih et al., 2024).

To date, Saydam et al. (2022) have examined the impact of leeway angles on ship resistance at 5-degree intervals within a range of 0°–15°, combined with heel angles of 5° and 10°. They concluded that the influence of heel on resistance can be considered negligible up to 10°. The leeway angle was observed to increase the viscous component of resistance beyond 5°. Additionally, asymmetry in wave formation and pressure distribution resulted in an increase in the normal component of resistance as leeway angle grew. Consequently, it was noted that the hull's tendency to generate side force aligns with expectations, with the force increasing proportionally to the leeway angle. Separately, Zhang et al. (2024b) analysed leeway angles of 0°, +10°, and −10° in their study. For a 0-degree leeway angle, they utilised a static rudder angle ranging from −35 to +35° in 5-degree increments. Their findings showed that during straight-ahead motion, a rudder angle of 35° resulted in approximately a 20 % increase in total resistance. This increase was much more modest (approximately 2.5 %) for rudder angles up to 10°. When assessing the effect of a 10-degree leeway angle with the rudder at zero degrees, the resistance increase was limited to 30 %. The combined effect of a +10-degree leeway angle and a rudder angle resulted in an approximately 33 % increase in total resistance compared to the reference value. In addition, Reche-Vilanova et al. (2021) evaluated the impact of three different wind-assisted propulsion systems on the energy efficiency of ships under various operational conditions. Ship performance was assessed by considering factors such as velocity, wind speed and direction, as well as rudder angles of −20° and +20° at leeway angles of −10° and +10°. Rotor sails were determined to be the most efficient WAPS based on force generation per square meter of anticipated sail area, achieving 7.76 % normalised efficiency. Most recently, Hosseinzadeh et al. (2025) presented a high-quality experimental dataset for a model-scale KCS ship tested in calm water and waves, aimed at improving the understanding of hull-propeller-rudder interactions under various leeway, rudder, propeller, and wave conditions. The results obtained were used for comparison with performance data from both calm water and regular wave condition tests previously conducted by other researchers. Additionally, they asserted that defining a ship's hydrodynamic properties, supported by a comprehensive examination of vessels with WAPS, ultimately aids ship design optimisation for improved efficiency and reduced emissions.

In summary, leeway and rudder angles significantly impact ship resistance and manoeuvrability. Studies show that even modest leeway angles can significantly increase viscous resistance. Resistance typically increases with rudder angle, and combinations of leeway and rudder angles, further complicated by the propeller-rudder interactions, can lead to even greater resistance increases.

1.3. Paper contribution and outline

The main strength of this paper lies in its comprehensive verification methodology, which distinctively combines CFD simulations with model-scale experimental data and full-scale sea trial results provided by the ship's operating company, resulting in a more detailed verification than is often found in related literature. This study also performs an extensive parametric analysis of the combined impacts of various leeway and rudder angles on ship resistance, specifically measuring their influence on the wave-making resistance coefficient —a depth and focus not routinely seen in available literature. The study utilizes an advanced CFD methodology, adopting a numerical planar motion mechanism approach with the Dynamic Fluid Body Interaction (DFBI) model to accurately simulate ship motions (free to trim and sink for this study) in Star-CCM + version 18.04.008, and with a detailed verification analysis, thereby enhancing the reliability of its results on hydrodynamic forces. These factors combined offer substantial insights into optimising ships with wind-assisted propulsion.

The paper is organised as follows: Section 2 details the case ship, describes the methodologies for resistance calculation, and Section 3 outlines the validation and verification process. Section 4 presents the results and key findings. Finally, Section 5 offers conclusions and recommendations for future work.

2. Research methodology

The study leveraged data from sea trials and experimental fluid dynamics (EFD) methodologies to enhance the reliability of CFD analyses.

By benchmarking both numerical and experimental techniques, an efficient framework for ship performance analysis was developed.

2.1. Case study ship model

Fig. 1 illustrates the ship's hull, and the coordinate system used in this study. The coordinate system was defined according to the right-hand rule: the keel lies along the x-axis (bow in +x direction), the port side is +y, and +z extends upward (opposing gravity). Wind-assisted propulsion devices generate aerodynamic forces, including a lateral (side) force component resulting from the wind. This lateral force, applied at the device's position on the ship, creates a lever arm relative to the vessel's centre of gravity (CoG), thereby producing a yawing moment. This rotational moment alters the ship's heading, affecting its directional stability and potentially requiring rudder adjustments to maintain the desired course. Additionally, the technical specifications of the ship and its scaled model correspond to a 1:32 model-to-full scale ratio, are given in Table 1.

2.2. Resistance calculations

This section outlines the methods employed for the ship resistance analyses. A precise calculation of a vessel's resistance is essential for optimising both the design and operation. This includes a comprehensive analysis of complex hydrodynamic forces, with various approaches being established to tackle this issue. As mentioned above, this study emphasises the computational fluid dynamics methodology by highlighting the critical importance of experimental data gathered from towing tank tests and sea trials.

The towing tank experiments for the scale model were conducted in the University of Southampton's Boldrewood towing tank in 2024 (Garad et al., 2024). The facility measures 138 m in length, 6 m wide, and has a water depth of 3.5 m. The resistance experiments were conducted at two speeds (at 0.194 and 0.246 Froude numbers, corresponding to 1 m/s and 1.273 m/s, respectively), with the model towed in calm water for each case. Additionally, experimental uncertainty was evaluated at a model speed of 1 m/s through five repeated runs. Moreover, sea trials conducted by the ship operator at 1-knot speed increments (8–14 knots) provided real-world verification and a calibration basis for extrapolated model-scale results. Resistance tests at these speeds directly compared CFD and experimental results under conditions without leeway or rudder angles.

Table 1
The particulars of the case hull.

Particular	Value		Unit
	Ship	Model	
Displacement volume	5865	0.179	m^3
Draft amidships (T)	5.45	0.170	m
Waterline length (L_{WL})	87.10	2.722	m
Beam maximum	15.20	0.475	m
Wetted area	2049	2.001	m^2
Prismatic coefficient (C_p)	0.828		–
Block coefficient (C_b)	0.826		–
Maximum section area coefficient (C_m)	0.997		–

2.2.1. Dimensionless numbers

The fundamental distinction between model-scale and ship-scale is characterised by the Reynolds number (Re) in Eq. (1), where ρ is the density of fluid [kg/m^3], V is for the ship or model speed [m/s], L represents the characteristic length (ship or model) [m], and μ is used for the dynamic viscosity of the fluid [Ns/m^2]. For model-scale analysis, Re is around 10^6, and for ship-scale assessments, it is around 10^8.

$$Re = \frac{\rho V L}{\mu} \tag{1}$$

The Froude number (Fr), as indicated in Eq. (2), is another crucial dimensionless parameter in naval architecture, with g denoting the acceleration due to gravity.

$$Fr = \frac{V}{\sqrt{gL}} \tag{2}$$

Reynolds and Froude numbers ensure dynamic similarity between model tests and full-scale ships, making them vital for ship resistance calculations. Re drives viscous resistance scaling (Korkmaz et al., 2021), while Fr governs wave-making resistance scaling (Mikkelsen et al., 2019). Thus, extrapolating model test findings to predict full-scale ship resistance requires knowing Re and Fr (Elsherbiny et al., 2020).

For each CFD simulation case defined by a model speed, leeway angle, and rudder angle, the side force (F_Y) and yawing moment (M_z) on the model were obtained. All of these forces and moments were recorded as time histories (just as resistance is tracked over time). This approach captures detailed hydrodynamic properties of the ship's hull. Equations are given for Y' and N', describing the non-dimensional values of side force and yawing moment coefficients, respectively, in Eq. (3) and Eq. (4) (ITTC, 2024).

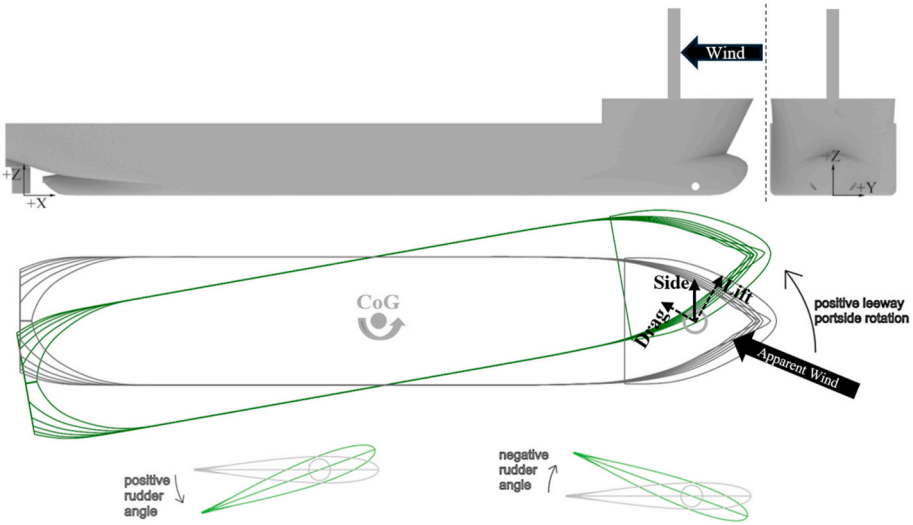

Fig. 1. The hull form of the ship and global coordinate system.

$$Y' = \frac{F_y}{(1/2)\rho U_C^2 TL} \tag{3}$$

$$N' = \frac{M_z}{(1/2)\rho U_C^2 TL^2} \tag{4}$$

where, U_C is for the carriage speed (that is called the overset region's advancing velocity for CFD) [m/s] and T represents the draft [m].

2.2.2. Extrapolation calculations

Despite extensive research and numerous experiments, scaling viscous forces remains a persistent challenge (Terziev et al., 2021). The International Towing Tank Conference (ITTC) recommends using a method that accounts for the 3D viscous effects on a ship's surface to achieve a more accurate evaluation of those forces. This approach utilizes the form factor (1+k), which is assumed to be consistent for both the model and the ship, regardless of the ship's speed.

$$C_{TS} = C_{FS}(1+k) + \Delta C_F + C_A + C_W + C_{AAS} \tag{5}$$

where.

C_{TS}: total resistance coefficient for ship
C_{FS}: frictional resistance coefficient for ship
ΔC_F: Roughness allowance
C_A: Correlation allowance
C_W: wave resistance coefficient
C_{AAS}: air resistance coefficient

$$C_W = C_{TM} - C_{FM}(1+k) \tag{6}$$

The ITTC-1957 frictional resistance coefficient is calculated using Eq. (7)

$$C_F = \frac{0.075}{\left(\log_{10} Re - 2\right)^2} \tag{7}$$

However, several methods are available for determining the frictional resistance coefficient. One of the most widely used is the Prohaska (1966) method, which employs low Froude number resistance data so that the wave-making component can be neglected (Purnamasari et al., 2022); the coefficient is then obtained from Eq. (8).

$$1+k = \frac{C_V}{C_F} \tag{8}$$

Another widely used approach is the Hughes formula for the frictional-resistance coefficient, presented in Eq. (9).

$$C_F = \frac{0.066}{\left(\log_{10} Re - 2.03\right)^2} \tag{9}$$

The form factor of the case study ship model was calculated using double body CFD analysis. Double body simulations employ a symmetry plane instead of a free surface, which inherently means the wave resistance coefficient is zero. Consequently, Eq. (6) is expressed as $C_{TM} = C_{FM}(1+k)$. For context, in multiphase simulations (which include a free surface), the total resistance coefficient is typically decomposed into pressure resistance (C_P) and frictional resistance (C_F); that is, $C_T = C_P + C_F$. In such cases, C_P includes contributions from both viscous pressure and wave generation. In the double body simulations discussed here, however, since $C_W = 0$, the total resistance consists of the viscous pressure resistance coefficient (C_{VP}) and the frictional resistance coefficient (C_F); $C_T = C_{VP} + C_F$ (Terziev et al., 2019). Eq. (10) was then used in this study to determine the form factor $(1+k)$.

$$1+k = C_{T_{double\ body}} \Big/ C_{F_{double\ body}} \tag{10}$$

2.2.3. Computational fluid dynamics methodology

The Navier–Stokes equations are partial differential equations that describe the motion of viscous fluids. However, solving these equations precisely is difficult, especially in turbulent flows. The Reynolds-averaged Navier–Stokes (RANS) equations form the basis of many numerical models used in ship-hydrodynamics studies. In the RANS approach, flow variables such as velocity and pressure are decomposed into mean and fluctuating components, and the governing equations are then written for the time-averaged quantities. This averaging procedure captures the effects of turbulence without requiring every instantaneous fluctuation to be resolved. While steady-state RANS offers only a coarse time-averaged picture of the flow, unsteady RANS (URANS) simulations capture the temporal evolution of turbulence in far greater detail. As noted earlier, the Reynolds-averaged Navier–Stokes equations were solved in this study with the commercial CFD package Star-CCM+ (CD-Adapco, 2023).

2.2.3.1. Computational domain and boundary conditions. The CFD boundary conditions were chosen to mimic the physical characteristics of the towing tank. However, the CFD analyses were themselves performed in a virtual tank domain replica measuring 6 m in width and 3.5 m in water depth. The fluid volume was configured to sustain a 50-s analysis period at each towing speed, featuring a 2-m air layer above the water. Domain lengths of 60 m and 74 m were used for Froude numbers 0.194 and 0.246, respectively, to replicate the carriage motion in the physical tank. To mirror the experimental setup, the side and bottom surfaces of the domain were modelled as no-slip walls (grey in Fig. 2). The area behind the hull was set as a pressure outlet (red) to allow the model's wake to exit. It should be noted that the wave pattern in the simulation was generated by the hull–fluid interaction at the free surface, not by the outlet boundary. The outlet's role is simply to terminate the domain and let waves exit without reflection; a 1.4 m damping zone was applied near the outlet to absorb outgoing waves. The bow-facing outer surface and the top surface (green surfaces) were designated as velocity inlets to establish a calm water condition. In this study, the ship's movement was managed using an overset mesh; therefore, the inlet boundaries for both water and air were assigned a velocity condition of 0 m/s, mimicking a captive towing tank experiment. Fig. 2 illustrates the ship's hull (black surfaces) along with the overset domain surrounding the model (yellow surfaces), and the other domains. The simulation employs an overset mesh in which a region containing the ship's hull translates along with the hull's movement. This moving region is superimposed onto a stationary background mesh that represents the entire computational domain. A key advantage of this method is the reduction of computational expense while maintaining fine mesh resolution near the hull and free surface.

2.2.3.2. Mesh generation, overset mesh and y^+ value selection. The trimmer mesh serves as an effective tool for simulating complex geometries in Star-CCM+. When implemented effectively, it significantly boosts the accuracy of fluid dynamics simulations and increases computational efficiency. To improve the accuracy and reliability of the simulation results, mesh elements were refined in areas where water and air interact, especially close to the ship hull and the free water surface. During this process, zones of volumetric mesh refinement (with varying extents) were established. Fig. 3 illustrates portions of the mesh structure used in this study (approximately 20 million cells for the *Fr* 0.194 case).

The representation of the CFD boundary layer is influenced by turbulence modelling. Pena et al. (2020) also observed that the selection of a turbulence model can significantly impact boundary layer predictions; however, the literature lacks definitive guidelines for choosing numerical modelling methodologies for ship boundary layers.

In this study, overset mesh technology was utilised to prevent mesh distortion during large-amplitude movements. In essence, the overset mesh serves as a numerical analogy to the towing tank's moving carriage, enabling analysis of vessel motions and performance under

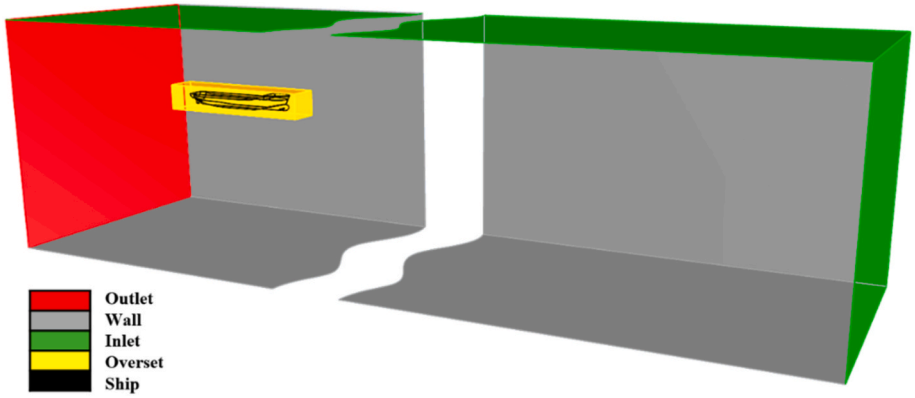

Fig. 2. Definition of boundary conditions.

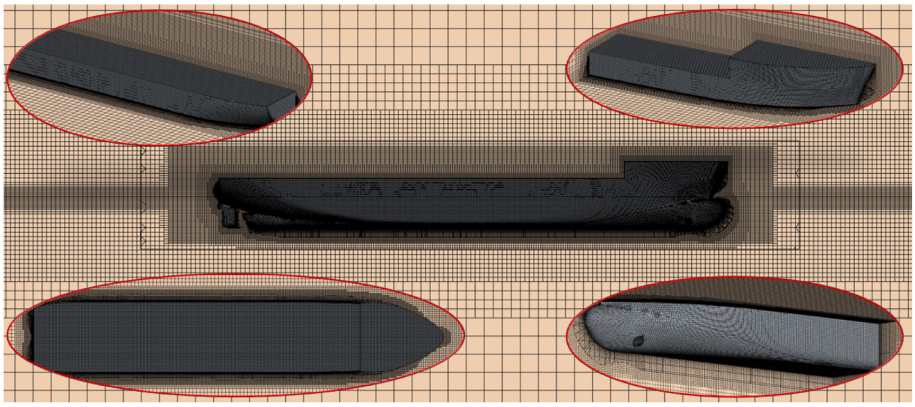

Fig. 3. Generated computational mesh.

various conditions.

The accurate selection of time step and y^+ values is essential to ensure the precision, stability, and efficiency of CFD simulations, particularly in scenarios that involve turbulence and wall-bounded flows, such as ship resistance analysis. The ITTC guidelines (ITTC, 2014) are expressed in terms of the non-dimensional wall distance of the first point from the wall, y^+, as illustrated in Fig. 4 for the ship's hull. Maintaining a uniform y^+ distribution on the hull is crucial for simulation accuracy, especially in resolving the boundary layer. In this study, the target y^+ (y^+ value of 30) was consistently achieved under all speed conditions, according to our numerical analysis.

Friction velocity (u^*):

$$u^* = \sqrt{\frac{T_w}{\rho}} \tag{11}$$

Non-dimensional wall velocity (u^+):

$$u^+ = \frac{u}{u^*} \tag{12}$$

Non-dimensional wall distance (y^+):

$$y^+ = \frac{\rho u^* y}{\mu} \tag{13}$$

where, T_w is the skin friction, u is the local velocity, μ is the dynamic viscosity of the fluid, and y is for the wall-normal coordinate.

The choice of turbulence model and the associated wall treatment

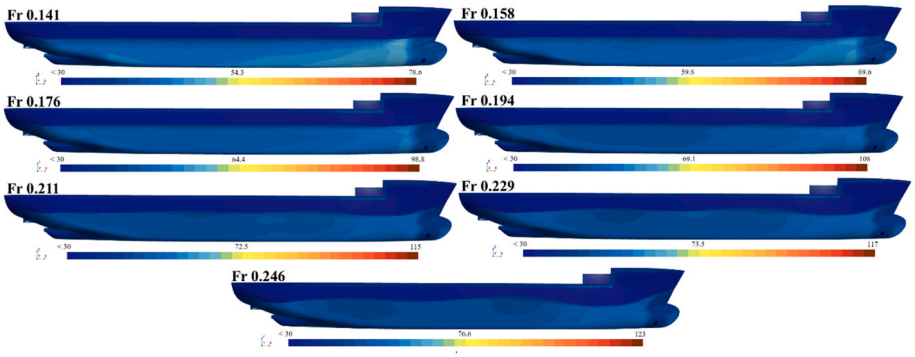

Fig. 4. Distribution of y^+ values on the hull surface.

strategy is directly dependent on the required near-wall mesh resolution, y^+. Since the use of wall functions is preferred, a relatively coarse mesh targeting $y^+>30$ is appropriate, positioning the first cell within the log-law region. This decision reflects a balance between near-wall accuracy requirements and computational cost, and verification of the resulting y^+ values after simulation is essential to ensure compatibility with the selected turbulence modelling approach.

2.2.3.3. Physics modelling. The finite volume method was utilised to conduct ship resistance analyses using Star-CCM+, which offers a high-resolution interface-capturing (HRIC) methodology that improves the characterisation of the free surface. Consistent alignment between the overset domain and the towing tank domain ensures accurate tracking of the ship's position, providing an ideal framework for modelling ship-water interactions.

The Volume of Fluid (VOF) method, in conjunction with the K-ε Realizable turbulence model, offers a strong foundation for simulating intricate multiphase flows (Atreyapurapu et al., 2014), where precise modelling of interfacial dynamics and turbulent mixing is crucial. The VOF method accurately captures the changes in the fluid interface, while the K-ε Realizable model reliably presents (or predicts) turbulent stresses. Together, they provide valuable insights into flow behaviour, supporting the optimisation of designs across various engineering applications.

Resistance analyses in calm water conditions for the ship model were conducted using water properties with a density of 999.1026 kg/m^3 and a dynamic viscosity of 0.001138 *Pa.s*. Air properties were specified as a density of 1.18415 kg/m^3 and a dynamic viscosity of $1.855x10^{-5}$ *Pa.s*.

As mentioned previously; to accurately replicate the ship's dynamics, the Dynamic Fluid Body Interaction (DFBI) model was employed, allowing the vessel to trim and sink freely. This approach enables the RANS solver to calculate the hydrodynamic forces and moments acting on the hull, which are then used to solve the rigid body motion equations and update the vessel's position and orientation accordingly.

2.2.3.4. Time step selection and CFL calculations. To ensure accurate turbulence modelling, all simulations employed a fixed time step of 0.004 s and a second-order time-discretisation scheme. In comparable studies, the time step value is typically limited to an upper limit of $0.0035L/U$, where L is for model length [m] and U defines model speed [m/s]. The time step employed in this study adheres to this guideline, being below the upper limit for the Froude numbers of 0.194 and 0.246.

The Courant–Friedrichs–Lewy (CFL) number –a dimensionless ratio of local flow velocity to numerical-grid travel distance– is a key stability criterion for time-dependent simulations. A value below 1 is generally recommended, and this guideline was observed in the present study (see Table 2). The exact upper limit, C_{max}, can vary with the problem type, as indicated by Eq. (14) and the ITTC guidelines (ITTC, 2014).

$$\frac{\Delta t|\overline{u}|}{\Delta x} < C_{max} \tag{14}$$

where.

Table 2
Numerical solution parameters related with CFL number.

V_s [knot]	V_m [m/s]	Δt [s]	Δx [m]	CFL
8	0.727	0.004	0.00625	0.466
9	0.818	0.004	0.00625	0.524
10	0.909	0.004	0.00625	0.582
11	1.000	0.004	0.00625	0.640
12	1.091	0.004	0.00625	0.698
13	1.182	0.004	0.00625	0.757
14	1.273	0.004	0.00625	0.815

Δt: is for the time step [s]
$\overline{u}$: is for the local velocity [m/s]
Δx: is for the mesh length on the longitudinal direction [m]

For consistency with the base-mesh dimensions adopted in the uncertainty analysis (see Verification Study), the streamwise cell size was fixed at $\Delta x = 0.00625\ m$. At this resolution, the chosen time step keeps the CFL number safely below 1.

3. Verification study

The convergence test is an essential element of computational modelling. It quantifies the uncertainties in model inputs, tracks how they propagate through the simulation, and assesses their impact on the results' reliability. Over the years, many researchers have proposed strategies to reduce numerical discrepancies (Coleman et al., 2001; Eça et al., 2010; Roache, 1998; Wackers et al., 2017; Wilson and Stern, 2002).

A series of geometrically comparable grids are necessary to estimate numerical convergence check, ensuring consistent grid attributes and a proportional refinement ratio throughout the computational domain. Generating a succession of embedded grids by coarsening a fine grid or refining a coarse grid is feasible with grid generators, and an example of this series is shown in Fig. 5 (ITTC, 2021).

In applying convergence test to the CFD analysis, we systematically refined the mesh (see Table 3) and used four time steps (0.008 s, 0.00528 s, 0.004 s, 0.0032 s), resulting in a total of 16 simulations. The base mesh size was varied (with corresponding adjustments to surface mesh and boundary layer settings) to produce a series of hull mesh configurations. Notably, we kept the local hull surface mesh properties constant across these configurations, so any differences in results reflect mesh coarseness. As expected, coarser meshes yielded results that diverged more from the fine-mesh solution (the objective baseline). The refinement process used for the base mesh size is similarly applied to the time step values to assess the impact of the computational time step on the results.

The total resistance values [N] for the model ship operating at a *Fr* 0.194, with a leeway angle of 0° and a rudder angle of 0°. Table 4 lists the total resistance values obtained for each mesh/time-step combination, and Fig. 6 compares the resistance results across different mesh densities to illustrate grid convergence.

Fig. 6 is provided to help visualize and compare the resistance results for the different mesh and time-step parameters in the convergence test.

To evaluate the effect of mesh density on the accuracy of solutions in numerical analyses, the grid convergence index (GCI) is recommended by Celik et al. (2008). In this study, four distinct mesh structures were created for the convergence analysis. To assess solution convergence, the group of mesh structures M3 (coarse), M2 (medium), and M1 (fine) were analysed, and an M0 (extra-fine) mesh was generated for cases where the convergence criteria were not satisfied. Similarly, a finer time step of 0.0032 s was used as a reference to assess convergence against larger time steps (0.008 s, 0.00528 s, and 0.004 s). This approach ensured that the numerical solution was convergent. Subsequently, the results related to solution accuracy were determined.

Upon acquiring the aforementioned solutions, one can ascertain if the solution converges monotonically, oscillates, or diverges. This is executed according to the convergence ratio, as indicated in Eq. (15) (Celik et al., 2008).

$$R = \varepsilon_{21}/\varepsilon_{32} \tag{15}$$

where, f_1, f_2 *and* f_3 are the results and changes between medium-fine ($\varepsilon_{21} = f_2 - f_1$), and changes between coarse-medium ($\varepsilon_{32} = f_3 - f_2$). The convergence conditions defined by the (ITTC, 2021).

- for $0 < R < 1$; Monotonic convergence,

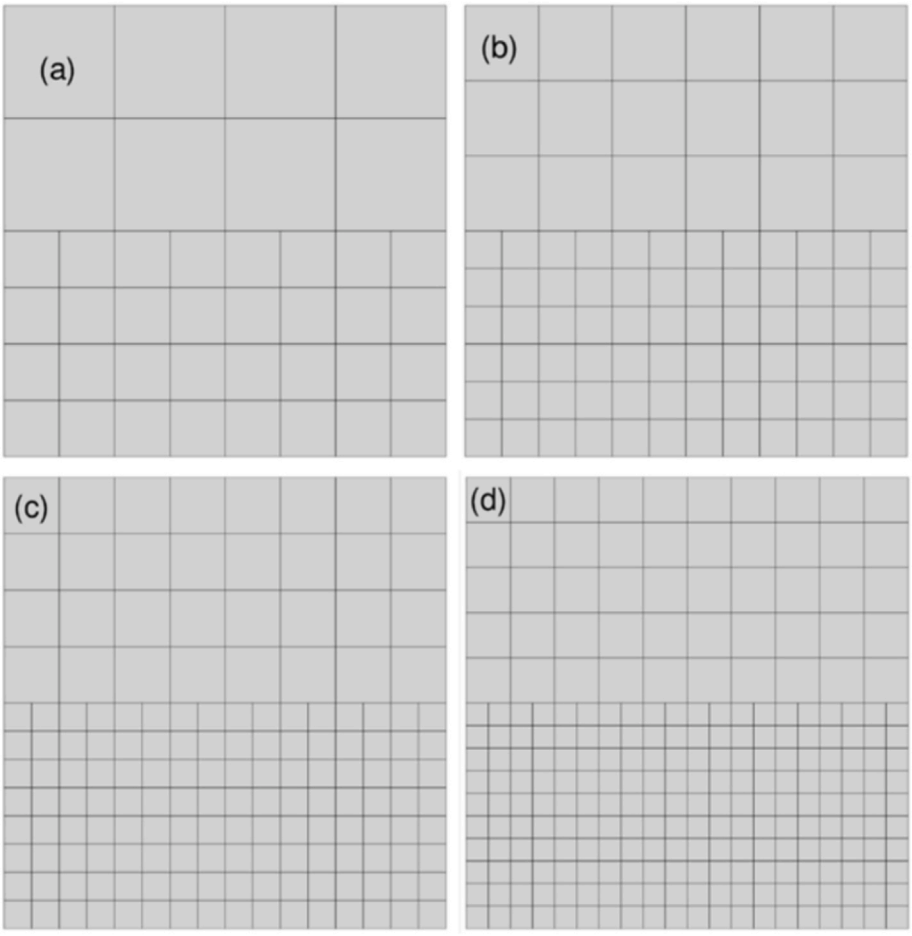

Fig. 5. Example mesh structure cases from coarser (a) to finer (d) (ITTC, 2021).

Table 3
Defined mesh properties of the convergence test for CFD analysis.

Mesh label	Mesh name	Base mesh sizes [m]	Total number of mesh
M3	Coarse mesh	0.500	5,126,579
M2	Medium mesh	0.350	9,754,971
M1	Fine mesh	0.250	20,196,960
M0	Extra-Fine mesh	0.175	42,186,892

Table 4
Resistance values, as Newton, obtained by convergence test of CFD parameters.

Base mesh sizes [m]	Time steps [s]			
	0.00800	0.00528	0.00400	0.00320
0.500	6.458	6.639	6.700	6.682
0.350	5.863	5.930	5.826	5.907
0.250	5.613	5.543	5.501	5.490
0.175	5.546	5.505	5.496	5.567

- for $R < 0$; Oscillatory convergence,
- for $R > 1$; Divergence.

To calculate the order of accuracy (p), Eq. (16) is given (Celik et al., 2008).

$$p = \frac{1}{\ln r}\left|\ln\left|\varepsilon_{32}/\varepsilon_{21}\right| + q(p)\right| \tag{16}$$

where the function $q(p) = 0$ for uniform refinement ratio, for the non-uniform refinement ratio it is given in Eq. (17).

$$q(p) = \ln\left(\frac{r_{21}^{p} - s}{r_{32}^{p} - s}\right) \tag{17}$$

where $s = sign(\varepsilon_{32}/\varepsilon_{21})$, refinement ratios between medium-fine (r_{21}^{p}) and coarse-medium (r_{32}^{p}). Then, the calculation of extrapolated solution is predicted by Eq. (18).

$$f_{ext} = (r_{21}^{p} f_1 - f_2) / (r_{21}^{p} - 1) \tag{18}$$

For grid convergence index, Eq. (19) was given.

$$GCI_{21} = 1.25\left|\frac{f_1 - f_2}{f_1}\right| \Big/ (r_{21}^{p} - 1) \tag{19}$$

The objective of this investigation is to analyse the influence of base mesh size and time-step on convergence assessment, leading to the derivation of the values presented in Table 5. The results indicate that the grid convergence has a *GCI* value of 6.90 %, accompanied by a *GCI* of 2.98 % for time-step convergence. This shows that the sufficient convergence criterion was reached by M3, M2, and M1 meshes, and the time step values of 0.008 s, 0.00528 s, and 0.004 s. It is important to acknowledge that the implementation of the GCI procedure results in the generation of an extrapolated solution. The extrapolated solution is commonly known as the mesh-independent solution. Nevertheless, it is inappropriate to consider this value (f_{ext}) as the definitive solution. This is due to the inability to establish that such solutions adhere to the principles of conservation laws.

The convergence study conducted using various parameter values to assess solution sensitivity, utilised a coarsest base mesh size of 0.500 m

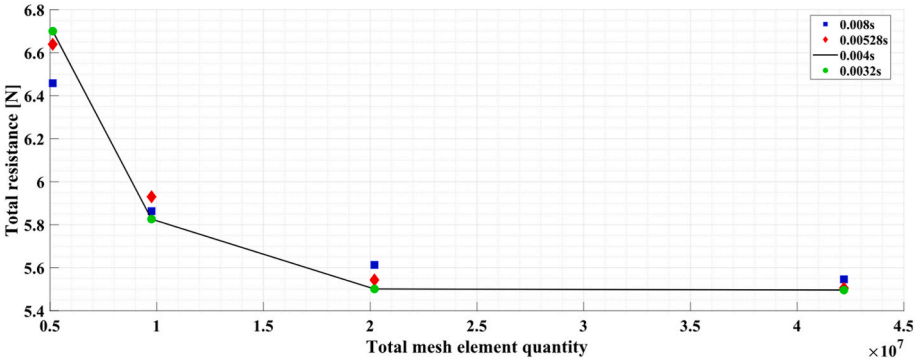

Fig. 6. Comparison of resistance values for convergence check.

Table 5
Grid and time step convergence study for total resistance.

	R_t for mesh base size convergence (with monotonic convergence)	R_t for time step convergence (with monotonic convergence)
r_{21}, r_{32}	2.0; 1.9	1.32; 1.5
f_1	5.501	5.501
f_2	5.586	5.543
f_3	6.700	5.613
R	0.372	0.600
p	1.444	0.628
q	0.170	−0.476
f_{ext}	5.197	5.370
GCI_{21}	6.90 %	2.98 %

and the finest base mesh size of 0.175 m, in accordance with ITTC recommendations. It is evident that as the mesh size decreased, discrepancies between results diminished, demonstrating mesh independence. When examining the impact of the time step on the solution, it was observed that the results remained largely consistent. However, the impact of the time step increased as the base mesh size increased (i.e., mesh became coarser). Conversely, this impact was minimal in analyses performed with smaller mesh units.

The results were comparable across simulations conducted with time steps of 0.004 s and 0.0032 s for a base mesh size of 0.250 m. Notably, using a time step of 0.004 s instead of 0.0032 s for the same base mesh size resulted in a 25 % reduction in overall solution time. Additionally, as the mesh is refined (i.e., base mesh size decreases and the total number of mesh elements increases), the computational time required for each phase would approximately double with each significant refinement step. Taking these factors into account, a base mesh size of 0.250 m and a time step of 0.004 s were deemed appropriate for this study.

As mentioned in Section 2.2.2, the double body model was to determine the form factor for the extrapolation studies and to calculate the friction resistance coefficients at model scale. The form factors obtained at different speed conditions are presented in Fig. 7. For subsequent calculations, the average form factor value of 1.33 was used.

This research investigates the hydrodynamic behaviour through the application of computational fluid dynamics simulations alongside towing tank experiments, specifically validating Froude numbers of 0.194 and 0.246. Seven different speeds were evaluated at both ship scale and model scale (Table 6). The corresponding Reynolds numbers and friction coefficients were calculated using Eq. (1) and Eq. (9), respectively.

Fig. 8 shows the resistance coefficients obtained from CFD for the zero-leeway, zero-rudder case. As speed (Fr = 0.141–0.246) increases, the friction coefficient C_F falls, whereas the wave-making resistance coefficient C_W rises. These opposing trends almost cancel, producing the nearly horizontal curve observed for the total-resistance coefficient. The rise in C_W—which exceeds the compensating drop in C_F—is linked to the hull form, especially the geometry of the forebody at the first point of water contact. The combined evolution of C_W and C_F therefore constrains the ship's energy-efficient operating speed.

Fig. 9 compares resistance values obtained by three methods: CFD, EFD, and sea trials. CFD and EFD results are shown at both model scale and full scale (the latter extrapolated as described in Section 2.2.2), whereas sea-trial data are available only at full scale. Because the sea trials reflect the vessel's true operating conditions, they provide the reference for estimating the main engine's instantaneous power demand. Accordingly, the numerical and experimental parameters must be selected so that model-scale results extrapolate realistically to full scale. In the present study, the extrapolated CFD predictions agree closely with the sea-trial measurements, and the model-scale CFD results differ from the EFD data by no more than approximately 10 %. This agreement confirms that the chosen modelling parameters fairly represent real-world conditions.

Table 7 compares full-scale resistance values derived from the three approaches—extrapolated CFD, extrapolated EFD, and sea-trial measurements. The EFD data reported by Garad et al. (2024) were used to calibrate the CFD model, and the side-by-side evaluation of calibrated

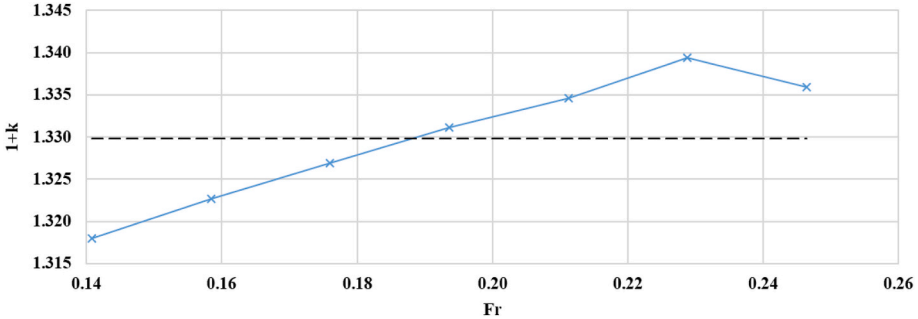

Fig. 7. The form factor values at different speed conditions.

Table 6
Description of the analysis cases and some key parameters.

Case	Fr	V_S [knot]	V_M [m/s]	Re (ship)	Re (model)	C_{FS}	C_{FM}
1	0.141	8	0.727	3.014E8	1.74E6	0.001587	0.003723
2	0.158	9	0.818	3.391E8	1.96E6	0.001562	0.003635
3	0.176	10	0.909	3.767E8	2.17E6	0.001540	0.003558
4	0.194	11	1.000	4.144E8	2.39E6	0.001521	0.003490
5	0.211	12	1.091	4.521E8	2.61E6	0.001504	0.003431
6	0.229	13	1.182	4.898E8	2.82E6	0.001488	0.003377
7	0.246	14	1.273	5.274E8	3.04E6	0.001474	0.003328

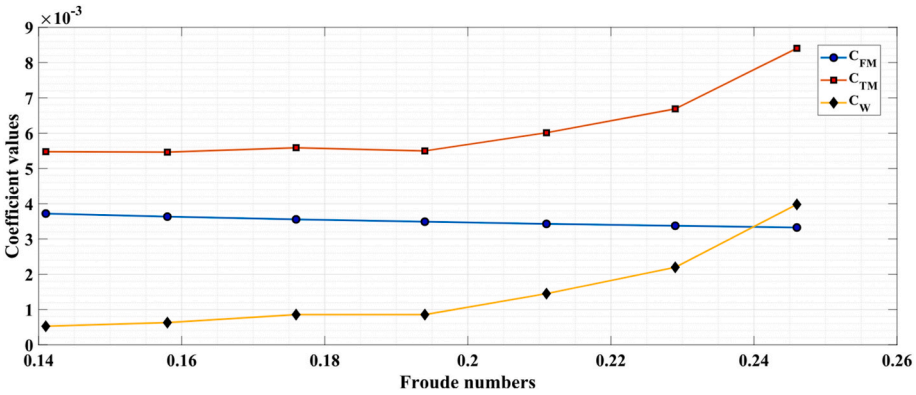

Fig. 8. Resistance coefficients of the model ship at a range of speeds, derived from CFD analysis (rudder and leeway angles are 0°).

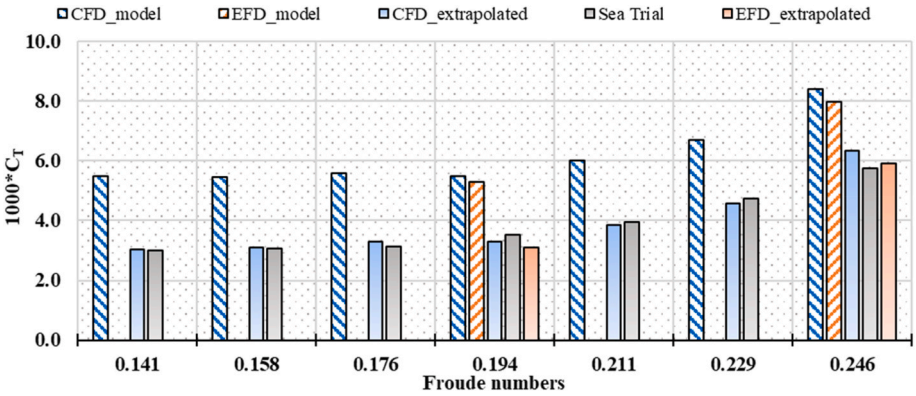

Fig. 9. Total resistance coefficients.

Table 7
Total resistance value differences at ship scale.

Case	Model-scale	Full-scale	
	Difference between CFD and EFD [%]	Difference between CFD and Sea Trials [%]	Difference between EFD and Sea Trials [%]
1	–	1.19	–
2	–	1.42	–
3	–	5.18	–
4	6.38	−7.08	−12.64
5	–	−2.15	–
6	–	−3.57	–
7	7.40	−10.26	2.67

CFD predictions, EFD values, and sea-trial results enables robust conclusions. In a comparative analysis of EFD and CFD methodologies, it was observed that the CFD approach yielded resistance values 6.38 % higher than those of EFD at a *Fr* 0.194, and 7.40 % higher at a *Fr* 0.246. When comparing both methods against sea trial data, the CFD results aligned more closely with real-world measurements at $Fr = 0.194$, whereas the EFD method showed better agreement at $Fr = 0.246$.

4. Results and discussion

4.1. Ship resistance in model and full scales

To achieve the study's objectives, we defined an analysis matrix that produced 41 distinct resistance values at each speed. These values were resolved along the x- and y-axes, representing the longitudinal and lateral resistance components, respectively. The data correspond to five different leeway angles (0°, 2.5°, 5°, 7.5°, and 10°) and nine different rudder angles (−20°, −15°, −10°, −5°, 0°, 5°, 10°, 15°, and 20°). The resistance values were obtained through CFD analyses conducted at Froude numbers, 0.194 and 0.246. Fig. 10 presents the total resistance increase ratios at $Fr = 0.194$ and 0.246. In Fig. 10, each bar chart indicates the increase in total resistance for various combinations of rudder and leeway angles, relative to the reference case (0° leeway, 0° rudder). Using the zero-angle case as a baseline allows a comprehensive evaluation of hydrodynamic behaviour under different operating conditions.

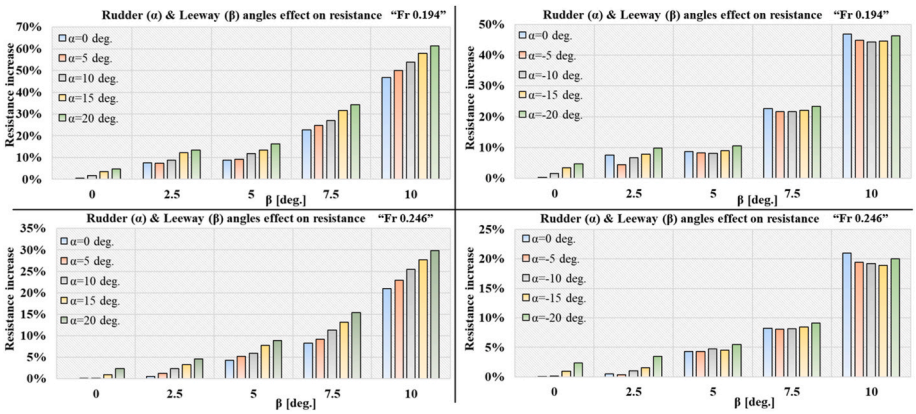

Fig. 10. Total resistance-increase ratios at model scale (Fr = 0.194 and 0.246).

The reference values are derived from the CFD analyses conducted without rudder or leeway angle, specifically at *Fr* 0.194 and 0.246. The data indicate that even with zero leeway, deflecting the rudder increases the longitudinal (x-axis) resistance, primarily due to the rudder's added drag (angle of attack effect). For instance, at a rudder angle of 20°, the total resistance increased by about 5 % at $Fr = 0.194$, and the lateral (y-axis) force contributed approximately 20 % of the total resistance (compared to the calm-water case).

With the rudder fixed at 0°, any non-zero leeway causes added resistance. For example, at 5° leeway (approximately corresponding to 1 m/s model speed), the longitudinal resistance increases by ~9 %, and at 10° leeway it increases by nearly 50 %. Based on these findings, limiting leeway to about 5° or less is advisable, as this keeps resistance increases below about 10 % (in model-scale results).

Laterally (y-axis), at $Fr = 0.194$ with rudder angle 0°, a leeway of 5° generates a side-force resistance component approximately 70 % as large as the reference resistance. At 10° leeway, this lateral resistance component grows to approximately 190 % of the reference case resistance.

Extrapolation is used to predict a full-scale vessel's resistance performance based on model-scale CFD results. This process accounts for changes in flow mechanics and turbulence characteristics at the much higher Reynolds numbers of a real ship. Accurate extrapolation is crucial for reliable ship design and performance prediction, and it helps minimise the uncertainties of relying solely on model tests.

In this study, we extrapolated the model-scale CFD results to full scale to understand how ship size affects the findings. Fig. 11 was generated to estimate the impact of leeway and rudder changes on full-scale propulsion and total resistance. It shows that increasing leeway above about 5° causes a significant rise in total resistance (consistent with the findings of Hosseinzadeh et al., 2024). This means the benefits of the wind-assisted propulsion system become limited at higher leeway angles, indicating that additional measures or design adjustments would be needed to maintain efficiency at full scale.

4.2. Wave-making resistance

In ship hydrodynamics, accurately capturing the free-surface flow is essential for examining wave-making resistance and pressure distribution around a moving hull. Precise modelling of the free surface leads to better predictions of resistance, which is crucial for design and performance analysis. Fig. 12 illustrates the free surface distributions for various combinations of leeway and rudder angles obtained from CFD simulations at $Fr = 0.246$. The results demonstrate that increasing leeway angles (0°, 5°, and 10°) introduce greater asymmetry in the wake patterns, highlighting the influence of lateral flow effects. Similarly, larger rudder angles (e.g., ±20°) significantly amplify wake disturbances, altering the symmetry and strength of the vortices. The combined effects of leeway and rudder angles generate complex wake dynamics, with extreme cases such as Leeway 10°, Rudder −20° exhibiting the most pronounced free surface deformation. Neutral conditions (Leeway 0°, Rudder 0°) result in relatively symmetrical wake profiles, while deviations from these settings lead to progressively nonlinear interactions. These findings, captured effectively through the CFD simulations, provide valuable insights into the hydrodynamic behaviour of the hull and rudder, with implications for optimising ship performance and manoeuvrability.

The wave-resistance coefficient is a key metric in ship-resistance analysis because it quantifies the share of total resistance attributable to wave making as the vessel moves through water. This numerical measure reveals trends that are not evident from visual inspection of the free-surface wave pattern alone. Tables 8 and 9 list the corresponding

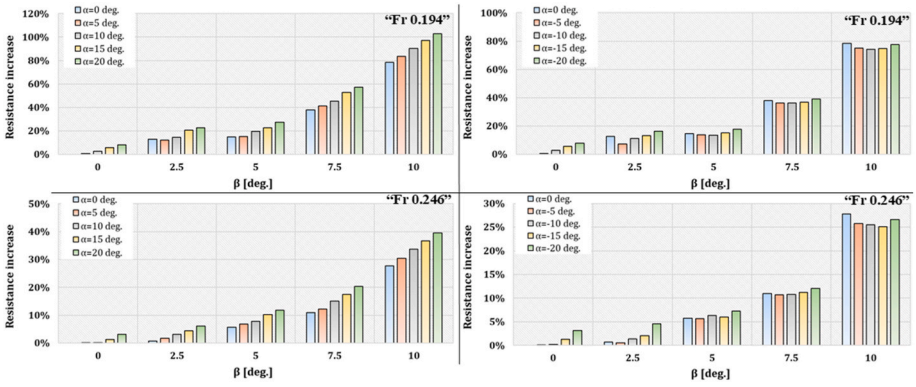

Fig. 11. Leeway (β) and rudder (α) angle effect on total resistance at ship scale.

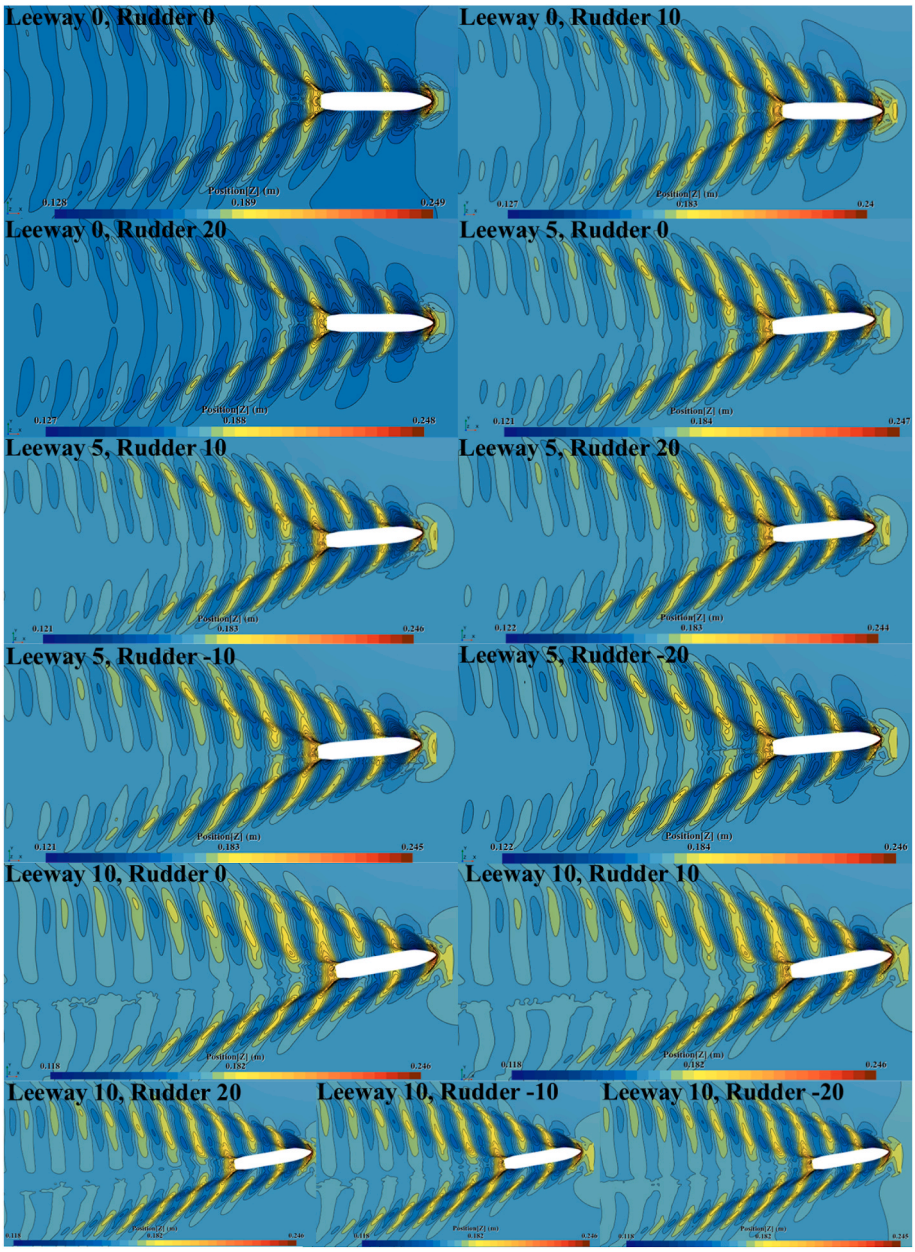

Fig. 12. Free surface distributions for selected cases, obtained from CFD simulations at $Fr = 0.246$

Table 8
Wave and total resistance coefficients in model scale at Fr 0.194 (values are multiplied by 10^3).

		Leeway angles [deg.]									
		0		2.5		5		7.5		10	
		C_W	C_{TM}	C_W	C_{TM}	C_W	C_{TM}	C_W	C_{TM}	C_W	C_{TM}
Rudder angles [deg.]	**−20**	–	–	1.396	6.038	1.441	6.083	2.145	6.787	3.402	8.045
	−15	–	–	1.291	5.933	1.354	5.996	2.069	6.711	3.308	7.951
	−10	–	–	1.230	5.872	1.303	5.945	2.045	6.687	3.294	7.937
	−5	–	–	1.100	5.742	1.314	5.956	2.051	6.693	3.323	7.966
	0	0.857	5.499	1.274	5.916	1.340	5.982	2.104	6.746	3.430	8.073
	5	0.879	5.521	1.260	5.902	1.360	6.002	2.216	6.858	3.602	8.245
	10	0.947	5.589	1.336	5.978	1.502	6.144	2.342	6.984	3.821	8.463
	15	1.046	5.688	1.532	6.174	1.596	6.238	2.594	7.236	4.044	8.686
	20	1.118	5.760	1.598	6.240	1.755	6.397	2.738	7.380	4.230	8.872

Table 9
Wave and total resistance coefficients in model scale at *Fr* 0.246 (values are multiplied by 10^3).

		Leeway angles [deg.]									
		0		2.5		5		7.5		10	
		C_W	C_{TM}	C_W	C_{TM}	C_W	C_{TM}	C_W	C_{TM}	C_W	C_{TM}
Rudder angles [deg.]	**−20**	–	–	4.270	8.696	4.442	8.868	4.743	9.170	5.665	10.092
	−15	–	–	4.108	8.534	4.360	8.787	4.693	9.119	5.573	9.999
	−10	–	–	4.066	8.492	4.380	8.806	4.666	9.093	5.598	10.024
	−5	–	–	4.013	8.440	4.339	8.766	4.661	9.087	5.613	10.039
	0	3.981	8.407	4.023	8.450	4.343	8.770	4.674	9.100	5.741	10.168
	5	3.984	8.410	4.088	8.514	4.418	8.845	4.756	9.183	5.909	10.336
	10	3.991	8.417	4.184	8.611	4.478	8.904	4.934	9.361	6.120	10.547
	15	4.063	8.490	4.260	8.687	4.633	9.059	5.087	9.514	6.306	10.732
	20	4.177	8.604	4.365	8.791	4.730	9.157	5.273	9.699	6.489	10.915

wave-resistance (C_W) and total-resistance (C_T) coefficients obtained from the longitudinal (x-direction) force component, showing how rudder and leeway angles affect C_W at Froude numbers of 0.194 and 0.246, respectively.

Figs. 13 and 14 plot the wave resistance coefficient as a function of rudder angle for *Fr* = 0.194 and 0.246, respectively, under various leeway angles. They illustrate that if the rudder is simply set to a positive angle equal to the positive leeway angle (achieving a static force equilibrium but not actually reducing the leeway), the ship continues to experience elevated resistance. In contrast, counteracting a positive leeway angle with a negative rudder angle slightly increases wave resistance, but this method can be more favourable. It realigns the ship's path closer to the undisturbed flow direction, avoiding the excessive turbulence and drag that occur with large rudder angles fighting a drift.

Molland et al. (2017) define total wave resistance as the component of resistance that arises from the energy a ship expends to generate waves while moving through water. A ship in motion produces waves primarily at the bow and stern. There are divergent waves (spreading outward, contributing relatively little to resistance) and transverse waves (with crests perpendicular to the direction of travel, being the main source of wave-making resistance). The ship's propulsion must supply energy to create these waves, effectively adding to the resistance opposing forward motion. Thus, the wave-making resistance quantifies the portion of energy lost to wave formation.

As shown in Fig. 12, the free-surface wave system is notably altered by the leeway angle. In neutral conditions (0° leeway, 0° rudder), the wave pattern resembles that of a conventional straight-running ship. Deviations from this (non-zero leeway or rudder) introduce asymmetry and additional wave-making. Figs. 13 and 14 delve further into these effects, illustrating how leeway and rudder angles quantitatively influence the wave resistance coefficient. For a small leeway angle, rudder angle has a limited effect on wave resistance. However, as the leeway angle grows, the combined effect of leeway and rudder deflection produces a much larger increase in overall wave resistance.

4.3. Side force and yawing moment

Side forces and yawing moments contribute significantly to ship resistance, as they require corrective measures—predominantly through rudder usage—which directly increases resistance. Therefore, Fig. 15 shows the corresponding side force coefficients at two different speed conditions related to five different leeway angles and nine different rudder angles. Increasing the leeway angle raises resistance in the x-axis direction and also generates a side force (y-axis), thereby increasing the total resistance. Consequently, the energy efficiency gains provided by the wind-assisted propulsion system may be affected. The ideal scenario is to navigate without a leeway angle. This zero-leeway condition might be approached by leveraging the aerodynamic forces of wind-assisted propulsion devices (sails, Flettner rotors, wing foils, etc.), which provide forward thrust while minimising lateral force. Additionally, structural design elements (e.g., optimized masts or aerodynamic fairings) can help reduce leeway by streamlining airflow and counteracting lateral drift. Furthermore, real-world hydrodynamic influences (wave direction, wave magnitude, currents) will cause a vessel's leeway angle to vary throughout a voyage. The results show that one can use rudder deflection to counteract (eliminate) a leeway angle. Nevertheless, it is evident that adjusting the rudder to reduce leeway will increase drag in both the x and y directions. All of these factors should be considered when operating a ship equipped with a wind-assisted propulsion system.

Fig. 16 illustrates the yawing moment coefficient curves for the model as a function of rudder angle at several fixed leeway angles (β), for *Fr* = 0.194 and 0.246. As expected, for a given leeway angle, yawing moment varies with rudder angle – approximately linearly for small rudder deflections. The sign and magnitude of the yawing moment correspond to rudder deflection direction, producing the necessary turning moment. Notably, leeway angle itself generates yawing moment: at $\beta > 0°$ with rudder 0°, the yawing moment is positive. Thus, a positive leeway angle induces an initial yawing moment that must be counteracted by a rudder-generated yawing moment in the opposite direction (e.g. a positive rudder angle yields a negative yawing moment to balance a positive yaw from leeway).

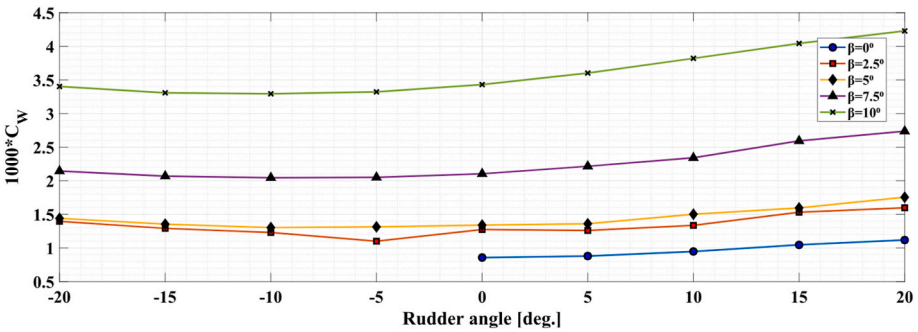

Fig. 13. Wave resistance coefficients at *Fr* 0.194 (β is for leeway angle degree).

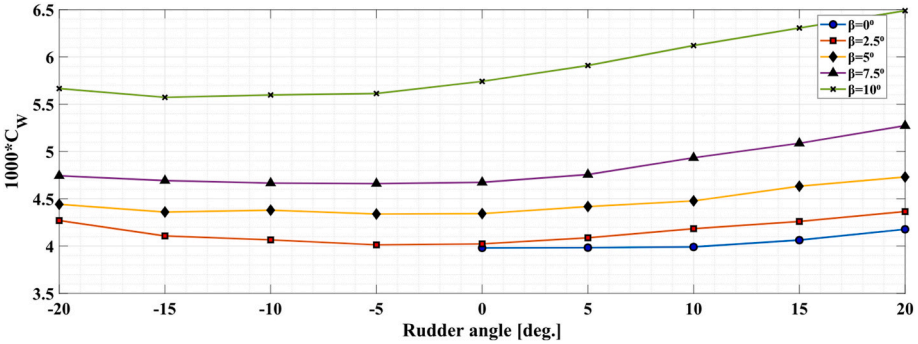

Fig. 14. Wave resistance coefficients at *Fr* 0.246 (β is for leeway angle degree).

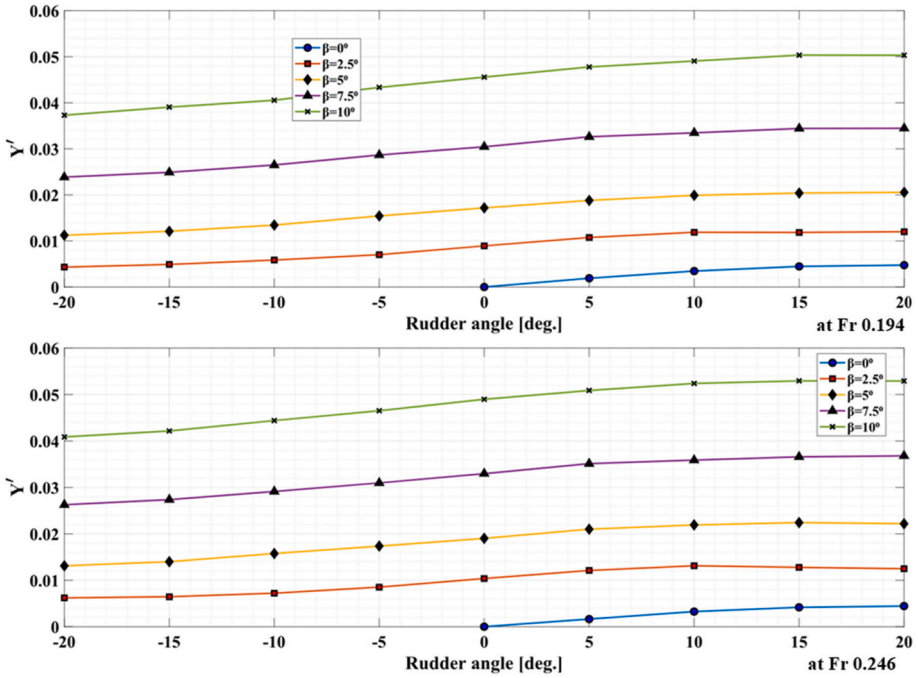

Fig. 15. Side force coefficients at *Fr* 0.194 and 0.246 for model scale.

Comparing the two speeds reveals that rudder effectiveness grows with speed. The higher Froude case ($V = 1.273$ m/s model speed) produces much larger yawing moments for the same rudder and leeway inputs – roughly scaling with the square of velocity. This underscores the complex relationship between control-surface deflection, a vessel's motion through water, and the resulting hydrodynamic forces. All of these factors are essential for analysing and predicting manoeuvring behaviour.

5. Conclusions

Wind-assisted propulsion offers significant potential to reduce fuel consumption in shipping. However, the lateral forces introduced by such systems pose challenges for course-keeping, making some leeway angle necessary to counteract drift. The objective of this study was to understand the effects of leeway angles on ship resistance by using multiple complementary analysis methods. This study has examined how leeway and rudder angles together influence the wave resistance coefficient for specific model speeds, emphasising the relationship between hydrodynamic forces and overall resistance. Using CFD simulations, the obtained results were compared against both experimental (EFD) data and full-scale sea trial data.

Ship resistance was evaluated at seven distinct speeds, Froude numbers ranging from 0.141 to 0.246, with resistance coefficients calculated at both the ship and model scales. We calibrated the CFD model using EFD results at $Fr = 0.194$ and 0.246 to ensure its accuracy for various leeway and rudder angles. The use of EFD data for calibration, combined with the availability of full-scale sea trial data, greatly strengthens the study. Sea trial data — while resource-intensive to obtain — provide essential real-world validation for the marine industry. Integrating these experimental insights (towing tank and sea trials) with CFD simulations broadened the scope of our analysis and enabled more precise decision-making. This integration also allowed us to assess scale effects between model and full scale and to refine extrapolation parameters. Overall, the combination of experimental, numerical, and full-scale methods proved advantageous in selecting appropriate computational techniques and parameters for the case ship, and it paves the way for future studies. Finally, the CFD simulations showed good agreement with both the experimental and sea trial data, validating our approach for assessing wind-assisted propulsion effects across different leeway and rudder angles.

For example, at $Fr = 0.194$ (increasing leeway to 2.5°, 5°, 7.5°, and 10° (with rudder fixed at 0°) caused x-axis resistance increases of approximately 7.6 %, 9.3 %, 22.7 %, and 46.8 %, respectively (model scale). In fact, at 10° leeway the total resistance was nearly double the zero-leeway reference. At the higher speed ($Fr = 0.246$), the x-axis

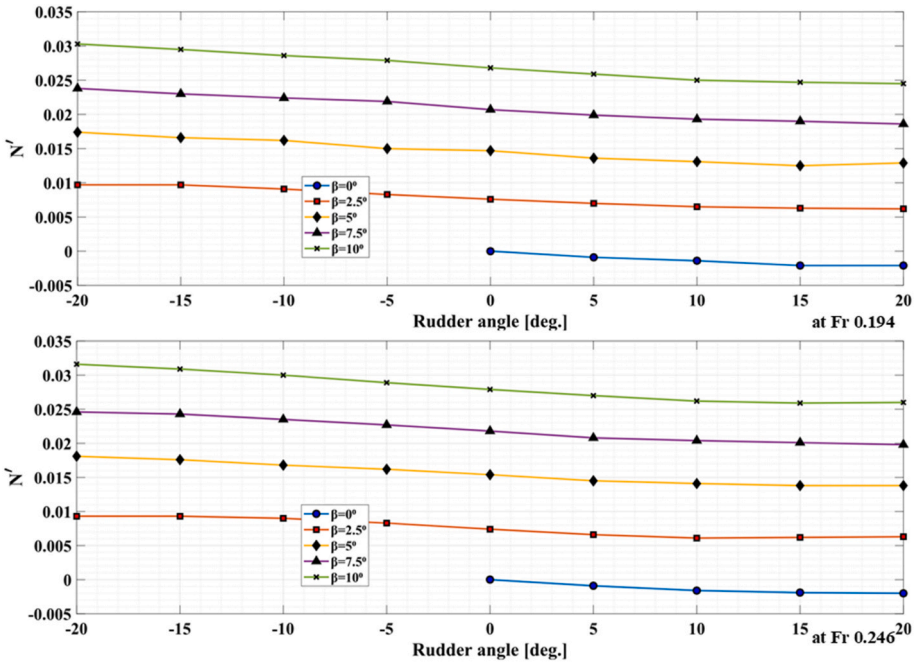

Fig. 16. Yawing moment coefficients as a function of rudder angle, at various fixed leeway angles.

(resistance) force increased more modestly: approximately 1 %, 4 %, 8 %, and 21 % for leeway angles of 2.5°, 5°, 7.5°, and 10°, respectively (again, rudder 0°, model scale). The study also revealed that certain rudder-leeway configurations can drastically reduce energy efficiency. For example, a +10° leeway combined with a +20° rudder increased the wave resistance to approximately four times the baseline (0°/0°) value, negating much of the propulsion benefit. On the other hand, adjusting the rudder in the opposite sense can mitigate wave resistance. A case with a +10° leeway and −20° rudder angle yielded a wave resistance coefficient of approximately 3.39×10^{-3}, nearly the same as that for +10° leeway and a 0° rudder. This outcome underscores that improper rudder-leeway alignment (e.g., rudder deflected in the same direction as drift) can maintain high resistance, whereas counteracting leeway with rudder can avoid added resistance growth.

This is a significant insight for enhancing ship performance. The misalignment between the rudder and leeway angles can maintain or increase wave resistance instead of reducing it. These findings support optimized ship design by balancing energy efficiency and stability, ultimately contributing to more sustainable maritime operations. By optimising rudder settings, it aims to reduce resistance, ultimately resulting in decreased operational costs and a reduced environmental impact.

Building on this work, future research could focus on: (1) simulating rudder–leeway interactions in more detail (and exploring hull design modifications that inherently limit leeway), (2) conducting extensive case studies or sea trials under diverse operating scenarios to validate efficiency gains, and (3) performing static drift tests to gather additional experimental data for manoeuvring analysis. Such static drift tests would strengthen the conclusions of this study by providing direct measurements of hydrodynamic forces at fixed leeway angles. In addition, deriving specific hydrodynamic coefficients via regression analysis is recommended to develop more comprehensive manoeuvring models and deepen understanding of the vessel's behaviour beyond what was covered here.

CRediT authorship contribution statement

Burak Göksu: Writing – original draft, Visualization, Validation, Software, Methodology, Formal analysis, Data curation, Conceptualization. **Suraj Garad:** Validation, Data curation. **Stefano Pandini:** Writing – review & editing, Resources, Project administration, Funding acquisition. **Edoardo Sirolla:** Writing – review & editing, Resources. **Robert Palin:** Writing – review & editing, Resources, Project administration, Funding acquisition. **Nicholas Townsend:** Writing – review & editing, Supervision, Resources, Project administration, Funding acquisition, Data curation. **Tahsin Tezdogan:** Writing – review & editing, Validation, Supervision, Resources, Project administration, Methodology, Investigation, Funding acquisition.

Declaration of competing interest

The authors declare that they have no known competing financial interests or personal relationships that could have appeared to influence the work reported in this paper.

Acknowledgments

The study presented in this paper was carried out under the research project: *Supercharging Wind Propulsion: Advancing Digital Tools in Maritime to Deliver Real-World Performance in a Next-Generation Wind Propulsion Design* (Project Number: 10093454). This project is part of the Clean Maritime Demonstration Competition Round 4 (CMDC4), funded by the UK Department for Transport (DfT) and delivered by Innovate UK. CMDC4 is part of the Department's UK Shipping Office for Reducing Emissions (UK SHORE) programme, a £206m initiative focused on developing the technology necessary to decarbonise the UK domestic maritime sector. The authors would like to acknowledge the support provided by Scotline Ltd. for their valuable contributions to this research.

References

Atreyapurapu, K., Tallapragada, B., Voonna, K., 2014. Simulation of a free surface flow over a container vessel using CFD. Int. J. Eng. Trends Technol. 18, 334–339. https://doi.org/10.14445/22315381/ijett-v18p269.

Bi, E., Li, S., Zhai, Z., Huang, B., Liu, X., Zhang, J., 2024. Analysis of wear characteristics of hydrodynamic seals during startup using 3D fractal characterization and study of opening performance degradation mechanism. Tribol. Trans. 67, 787–804. https://doi.org/10.1080/10402004.2024.2376109.

CD-Adapco, 2023. Simcenter STAR-CCM+ 2306 User Guide.

Celik, I.B., Ghia, U., Roache, P.J., Freitas, C.J., Coleman, H., Raad, P.E., 2008. Procedure for estimation and reporting of uncertainty due to discretization in CFD applications. J. Fluids Eng. ASME 130. https://doi.org/10.1115/1.2960953.

Charlou, M., Babarit, A., Gentaz, L., 2023. A new validated open-source numerical tool for the evaluation of the performance of wind-assisted ship propulsion systems. Mec. Ind. 24. https://doi.org/10.1051/meca/2023026.

Chou, T., Kosmas, V., Acciaro, M., Renken, K., 2021. A comeback of wind power in shipping: an economic and operational review on thewind-assisted ship propulsion technology. Sustain. Times 13, 1880. https://doi.org/10.3390/su13041880.

Coleman, H.W., Stern, F., Mascio, A. Di, Campana, E., 2001. The problem with oscillatory behavior in grid convergence studies. J. Fluid Eng. 123, 438–439. https://doi.org/10.1115/1.1363700.

Dupuy, M., Letournel, L., Paakkari, V., Rongère, F., Sarsila, S., Vuillermoz, L., 2023. Weather routing benefit for different wind propulsion systems. J. Sail. Technol. 8, 200–217. https://doi.org/10.5957/jst/2023.8.11.200.

Eça, L., Vaz, G., Hoekstra, M., 2010. A verification and validation exercise for the flow over a backward facing step. In: V European Conference on Computational Fluid Dynamics, pp. 14–17.

Elger, D.E., Bentin, M., Vahs, M., 2020. Comparison of different methods for predicting the drift angle and rudder resistance by wind propulsion systems on ships. Ocean Eng. 217, 108152. https://doi.org/10.1016/j.oceaneng.2020.108152.

Elsherbiny, K., Terziev, M., Tezdogan, T., Incecik, A., Kotb, M., 2020. Numerical and experimental study on hydrodynamic performance of ships advancing through different canals. Ocean Eng. 195, 106696. https://doi.org/10.1016/j.oceaneng.2019.106696.

Galić, S., Lušić, Z., Mladenović, S., Gudelj, A., 2022. A chronological overview of scientific research on ship grounding frequency estimation models. J. Mar. Sci. Eng. 10, 207. https://doi.org/10.3390/jmse10020207.

Garad, S., Townsend, N., Goksu, B., Tezdogan, T., 2024. CMDC4: Super Charging Wind Propulsion Model Scale Experimental Results v3, 0 (confidential).

Hosseinzadeh, S., Hudson, D., Turnock, S., Banks, J., 2024. Experimental investigation of the impact of leeway and rudder angles on the yaw moment balance for wind-propelled ships. In: Wind Propulsion 2024, pp. 291–302. London, UK.

Hosseinzadeh, S., Turnock, S., Lee, H., Olvera, R., 2025. Experimental dataset of a model-scale ship in calm water and waves. Data Brief 58, 111257. https://doi.org/10.1016/j.dib.2024.111257.

Issa, M., Ilinca, A., Martini, F., 2022. Ship energy efficiency and maritime sector initiatives to reduce carbon emissions. Energies 15, 7910.

ITTC, 2024. ITTC – Recommended Procedures and Guidelines Uncertainty Analysis for Manoeuvring Predictions Based on Captive Manoeuvring Tests.

ITTC, 2021. ITTC-recommended Procedures and Guidelines Uncertainty Analysis in CFD Verification and Validation Methodology and Procedures.

ITTC, 2014. ITTC – Recommended Procedures and Guidelines Practical Guidelines for Ship CFD Applications.

Korkmaz, K.B., Werner, S., Sakamoto, N., Queutey, P., Deng, G., Yuling, G., Guoxiang, D., Maki, K., Ye, H., Akinturk, A., Sayeed, T., Hino, T., Zhao, F., Tezdogan, T., Demirel, Y.K., Bensow, R., 2021. CFD based form factor determination method. Ocean Eng. 220, 108451. https://doi.org/10.1016/j.oceaneng.2020.108451.

Lu, S., Boucetta, D., Hoydonck, W. Van, Lataire, E., Delefortrie, G., 2023. Rudder hydrodynamics behind a propeller rotating ahead and astern. In: IOP Conference Series: Materials Science and Engineering, 012057. https://doi.org/10.1088/1757-899x/1288/1/012057.

Mikkelsen, H., Steffensen, M.L., Ciortan, C., Walther, J.H., 2019. Ship scale validation of CFD model of self-propelled ship. In: 8th Int. Conf. Comput. Methods Mar. Eng. Mar., 2019, pp. 730–741.

Molland, A.F., Turnock, S.R., Hudson, D.A., 2017. Ship Resistance and Propulsion: Practical Estimation of Ship Propulsive Power, second ed. Cambridge University Press. Cambridge University Press. https://doi.org/10.1017/9781316494196.

Oduro, P., Uzougbo, N.S., Ugwu, M.C., 2024. Navigating legal pathways: optimizing energy sustainability through compliance, renewable integration, and maritime efficiency. Eng. Sci. Technol. J. 5, 1732–1751. https://doi.org/10.51594/estj.v5i5.1152.

Park, I., Paik, B., Ahn, J., Kim, J., 2021. The prediction of the performance of a twisted rudder. Appl. Sci. 11, 7098. https://doi.org/10.3390/app11157098.

Pena, B., Muk-Pavic, E., Thomas, G., Fitzsimmons, P., 2020. An approach for the accurate investigation of full-scale ship boundary layers and wakes. Ocean Eng. 214, 107854. https://doi.org/10.1016/j.oceaneng.2020.107854.

Pradana, M.F., Noche, B., Ichsan, F.A., 2022. The pathway to decarbonization: Flettner rotor application in maritime logistics. In: Conference on Broad Exposure to Science and Technology 2021 (BEST 2021). Atlantis Press, pp. 72–78. https://doi.org/10.2991/aer.k.220131.012.

Prohaska, C.W., 1966. A simple method for evaluation of the form facter and low speed wave resistance. In: Proceedings of 11th ITTC, pp. 65–66.

Purnamasari, D., Maulana, F., Suwarni, E., 2022. A comparative of component resistance and form factor of four patrol boat. In: IOP Conference Series: Earth and Environmental Science, 012069. https://doi.org/10.1088/1755-1315/972/1/012069.

Reche-Vilanova, M., Hansen, H., Bingham, H.B., 2021. Performance prediction program for wind-assisted cargo ships. J. Sail. Technol. 6, 91–117. https://doi.org/10.5957/jst/2021.6.1.91.

Roache, P.J., 1998. Verification of codes and calculations. AIAA J. 36, 696–702. https://doi.org/10.2514/2.457.

Saydam, A.Z., Kucuksu, G.N., Insel, M., Gokcay, S., 2022. Investigation of the influence of wind-assisted propulsion devices on hull design. In: Sustainable Development and Innovations in Marine Technologies, pp. 211–216. https://doi.org/10.1201/9781003358961-27.

Schmidt, A., 2013. Ship 1 A wind-hybrid commecial cargo ship. In: Proceedings of the 4th Conference on Ship Efficiency, pp. 23–24.

Seddiek, I.S., Ammar, N.R., 2021. Harnessing wind energy on merchant ships: case study flettner rotors onboard bulk carriers. Environ. Sci. Pollut. Res. 28, 32695–32707. https://doi.org/10.1007/s11356-021-12791-3.

Song, C., Zhang, X., Zhang, G., 2022. Nonlinear innovation-based maneuverability prediction for marine vehicles using an improved forgetting mechanism. J. Mar. Sci. Eng. 10, 1210. https://doi.org/10.3390/jmse10091210.

Sun, Y., Su, Y., Hu, H., 2015. Experimental study and numerical simulation on hydrodynamic performance of a twisted rudder. Mar. Technol. Soc. J. 49, 58–69.

Sunarsih, Ndraha, A.K., Baidowi, A., 2024. Investigations of rudder-propeller clearance on thrust performance and flow field in vicinity of propeller. Pomorstvo 38, 153–163. https://doi.org/10.31217/p.38.1.12.

Talluri, L., Nalianda, D.K., Giuliani, E., 2018. Techno economic and environmental assessment of flettner rotors for marine propulsion. Ocean Eng. 154, 1–15. https://doi.org/10.1016/j.oceaneng.2018.02.020.

Terziev, M., Tezdogan, T., Demirel, Y.K., Villa, D., Mizzi, S., Incecik, A., 2021. Exploring the effects of speed and scale on a ship's form factor using CFD. Int. J. Nav. Archit. Ocean Eng. 13, 147–162. https://doi.org/10.1016/j.ijnaoe.2020.12.002.

Terziev, M., Tezdogan, T., Incecik, A., 2019. A geosim analysis of ship resistance decomposition and scale effects with the aid of CFD. Appl. Ocean Res. 92, 101930. https://doi.org/10.1016/j.apor.2019.101930.

Thies, F., Ringsberg, J.W., 2023. Retrofitting WASP to a RoPax vessel—design, performance and uncertainties. Energies 16, 673. https://doi.org/10.3390/en16020673.

Viola, I.M., Sacher, M., Xu, J., Wang, F., 2015. A numerical method for the design of ships with wind-assisted propulsion. Ocean Eng. 105, 33–42. https://doi.org/10.1016/j.oceaneng.2015.06.009.

Wackers, J., Deng, G., Guilmineau, E., Leroyer, A., Queutey, P., Visonneau, M., Palmieri, A., Liverani, A., 2017. Can adaptive grid refinement produce grid-independent solutions for incompressible flows? J. Comput. Phys. 344, 364–380. https://doi.org/10.1016/j.jcp.2017.04.077.

Wang, Y., Zhang, X., Lin, S., Qiang, Z., Hao, J., Qiu, Y., 2022. Analysis on the development of wind-assisted ship propulsion technology and contribution to emission reduction. In: IOP Conference Series: Earth and Environmental Science, 012012. https://doi.org/10.1088/1755-1315/966/1/012012.

Werner, S., Papanikolaou, A., Razola, M., Fagergren, C., Dessen, L., Kuttenkeuler, J., Santén, V., Steinbach, C., 2023. The orcelle project – towards wind-powered ships for deep sea cargo transport. In: SNAME Maritime Convention. SNAME. https://doi.org/10.5957/SMC-2023-089 p. D021S002R008.

Wilson, R., Stern, F., 2002. Verification and validation for RANS simulation of a naval surface combatant. 40th AIAA Aerosp. Sci. Meet. Exhib. 904. https://doi.org/10.2514/6.2002-904.

Yalama, V., Yakovleva, O., Trandafilov, V., Khmelniuk, M., 2022. Future sustainable maritime sector: fishing carriers and their adoption to the environmental regulations. Part I. Pol. Marit. Res. 29, 69–77. https://doi.org/10.2478/pomr-2022-0027.

Zhang, Y., Windén, B., Ojeda, H.R.D., Hudson, D., Turnock, S., 2024. Influence of drift angle on the propulsive efficiency of a fully appended container ship (KCS) using computational fluid dynamics. Ocean Eng. 292, 116537. https://doi.org/10.1016/j.oceaneng.2023.116537.